PHYSICAL REVIEW B **81**, 094427 (2010)

Ferromagnetic domain structures and spin configurations measured in doped manganite

J. Q. He,[1,2,*] V. V. Volkov,[1] M. Beleggia,[1,3] T. Asaka,[1] J. Tao,[1] M. A. Schofield,[1] and Y. Zhu[1]
[1]*Condensed Matter Physics and Material Science Department, Brookhaven National Laboratory, Upton, New York 11973, USA*
[2]*Department of Materials Science and Engineering, Northwestern University, Evanston, Illinois 60208, USA*
[3]*Center for Electron Nanoscopy, Technical University of Denmark, DK-2800 Kongens Lyngby, Denmark*

(Received 24 August 2009; revised manuscript received 5 November 2009; published 25 March 2010)

We report on measurements of the spin configuration across ferromagnetic domains in $La_{0.325}Pr_{0.3}Ca_{0.375}MnO_3$ films obtained by means of low-temperature Lorentz electron microscopy with *in situ* magnetizing capabilities. Due to the particular crystal symmetry of the material, we observe two sets of independent ferromagnetic twin variants, one of which was pinned by crystallographic twinning. The spin orientation and configuration of the domains were measured quantitatively using electron diffraction and electron holography, and verified with structural modeling. The observed deviation of spin orientations from the expected 90° head-to-tail configuration across the domain walls was attributed to the variation in the domains' aspect ratios as a result of the demagnetization field. Our study provides important insight on how the spin configuration coupled with the magnetic structure and the crystal symmetry might affect the magnetoresistivity under an applied magnetic field in a strongly correlated electron system.

DOI: 10.1103/PhysRevB.81.094427 PACS number(s): 75.47.Lx, 75.70.Kw, 61.72.Ff, 75.47.Gk

I. INTRODUCTION

Understanding the structure-property relationship of strongly correlated electron systems, including manganites, is one of the major challenges faced today in condensed-matter physics and materials science.[1] For example, the colossal magnetoresistance (CMR) effect in manganites usually accompanies transition from an insulator to metallic state, which is directly related to the charge-ordered antiferromagnetic (AFM) and metallic ferromagnetic (FM) phases.[2–5] Accordingly, magnetic domains and domain walls in the FM phase of these oxides may strongly affect not only their magnetic properties but also their electron-transport properties.[6–9] However, the electrical resistance of the magnetic domain walls critically rests upon the domain's configuration[10–12] because the reversal of magnetization at a domain wall in the interrupted perovskite crystal significantly scatters the charge carriers. A precise analysis and understanding of the magnetic microstructure is then vitally important for the fundamental understanding of advanced functional magnetic materials.

In this work, we focus on the orthorhombic $La_{0.325}Pr_{0.3}Ca_{0.375}MnO_3$ (LPCMO) pervoskite (*Pnma*) with $a=0.5441$ nm, $b=0.7676$ nm, and $c=0.5439$ nm lattice parameters.[5] LPCMO is a compound that exhibits a rich variety of physical phenomena, such as phase transitions and electronic-phase separation at low temperatures. Upon cooling, the material first undergoes a transition at $T=220$ K from the room-temperature paramagnetic phase to a charge-ordered AFM phase, followed at $T=160$ K by a state where ferromagnetism and charge ordering appear to coexist.[4] The magnetic domain configuration of these materials, and related ones, have been directly investigated by various methods.[13–16] Here, we employ high-spatial-resolution Lorentz transmission electron microscopy (LTEM) to observe the behavior of the magnetic domain configuration. Our observations shed light on the relationship between the magnetic structure and the effects of demagnetization fields arising from the finiteness of the domains.

II. EXPERIMENTAL PROCEDURES

Thin LPCMO films of ∼200 nm thickness were epitaxially grown on (010)-oriented single crystals of $NdGaO_3$ (NGO) using the pulsed laser deposition technique with $[010]_{LPCMO}\|[010]_{NGO}$, and $[001]_{LPCMO}\|[100]_{NGO}$ or $[001]_{NGO}$.[4] A KrF excimer laser operated at 10 Hz with an areal energy density of 2 J/cm^2 per pulse on the surface of a stoichiometrically sintered target of LPCMO was used for ablation. The oxygen pressure and the substrate temperature during the growth were held at ∼300 mTorr and 750 °C, respectively. Thin films were investigated by our JEM2100F-LM, a 200 kV field-emission electron microscope with a custom-made field-free objective lens (residual field ∼4 Oe).[17] *In situ* cooling experiments were conducted using a Gatan cooling stage filled with liquid nitrogen. TEM samples were prepared via standard mechanical thinning and polishing techniques to remove the substrate. The final thinning of the films was done using a Fischione ion miller with a single low-voltage Argon source at glancing angles and at liquid-nitrogen temperature.

III. OBSERVATIONS OF DOMAIN STRUCTURES

The LPCMO samples were examined by Lorentz electron microscopy over a large range of temperature. At 90 K, the FM phase dominated this sample and two sets of domain walls (denoted as "zigzag" and "twin" domain walls in Fig. 1) were clearly visible, slowly disappearing as the temperature increased approaching the FM to AFM transition (around $T=170$ K). The widths of twin domains did not change as a function of temperature, as might be expected, because the magnetic domain walls are pinned to the crystallographic (101) twin domain walls. Figures 1(a)–1(c) are Lorentz images of the LPCMO sample at 90 K showing the typical ferromagnetic domains viewed along the [010] direction taken, respectively, with nominal defocus of ∼−100 μm, +100 μm, and zero. The characteristic straight dark lines and bright lines in Figs. 1(a) and 1(b) represent the

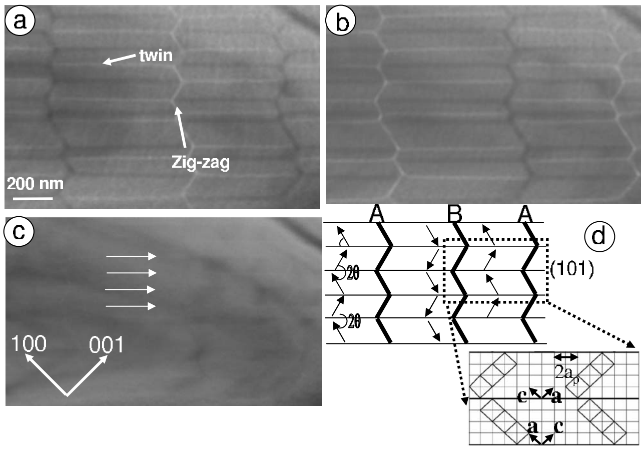

FIG. 1. Lorentz TEM images of LPCMO at 90 K. (a) Underfocus image, (b) over-focus image, and (c) in-focus image. The twin domain walls follow the crystallographic (101) twinning plane. (d) Schematic drawing of the local magnetic structure and crystal structure (enlarged part). The thick and thin black lines represent zigzag (180°) and twin (90°) domain walls, respectively. The twin ferromagnetic domains coincide with the crystal twinning lamellar structure of the sample.

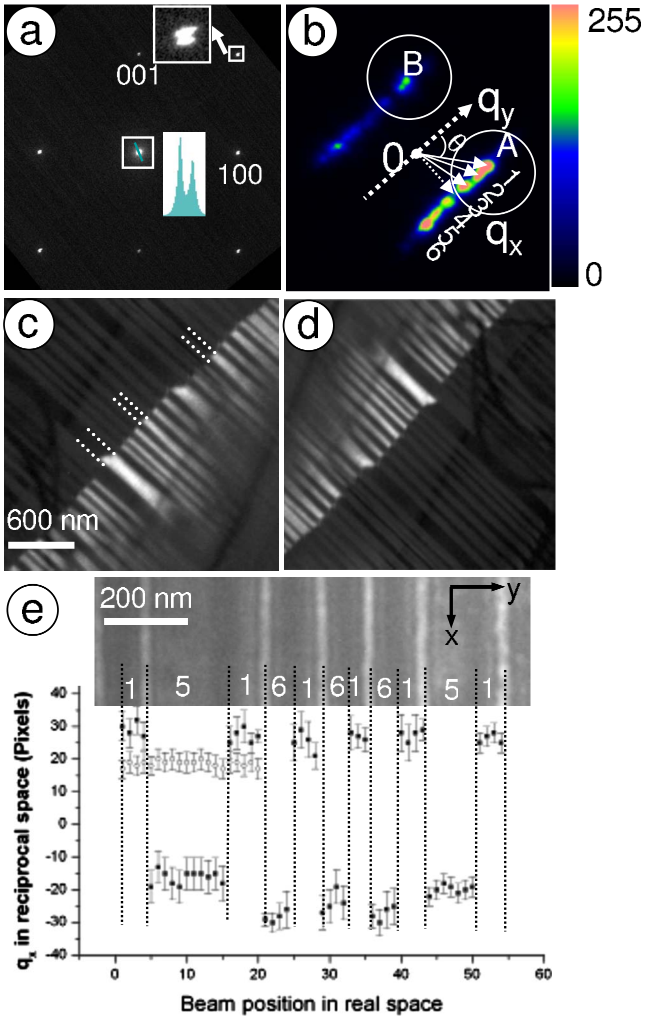

FIG. 2. (Color online) (a) The ED pattern of LPCMO at 90 K. Two boxed insets show the split intensity of transmitted beam and (101) Bragg reflection. (b) The magnetically split fine structure of transmitted beam, recorded using a large camera length of 15 m, shows two diffused lines of spotty intensities along the q_y direction. Two related Foucault images (c) and (d) were taken with the diffraction aperture at positions A and B in (b), respectively. (e) Two nanobeam diffraction scans across the twin domain structure. The deviation of (q_x,q_y) coordinates for diffraction spots versus scanning nanobeam position along (x,y) coordinates, respectively, parallel (open squares) and perpendicular (solid squares) to the twin domain walls in LPCMO.

divergent and the convergent magnetic domain-wall images, respectively. These contrast features have almost disappeared in Fig. 1(c); however, careful observation reveals some weak, wide, and straight contrast lines (marked by the white arrowheads) most likely due to diffraction contrast from the (101) crystallographic twin domains of the material. These magnetic domain walls coincide with the (101)-type twin boundaries.

Also, as evident in Figs. 1(a)–1(c), additional sets of magnetic domain walls were visible, with a characteristic zigzag pattern, labeled A, B, A in Fig. 1(d). These magnetic domain walls appear to separate 180° magnetic domains with antiparallel magnetization across the domain wall. The magnetic domains confined between the boundaries of twin lamellae are approximately 50–150 nm wide and the superposition of these two types of domain walls suggests that magnetization of individual magnetic domains should be aligned crystallographically with either [100] or [001] axes, the easy magnetization directions in LPCMO. Accurate measurement of the 2θ twist angles [see Fig. 1(a)] along the zigzag configuration revealed that the angles varied in the range [90°,120°] suggesting that the magnetization does not align exactly with the expected easy axes. A possible reason is that tensile strain in the film changes the orientation of the magnetization from [100] to somewhere in between [100] and [110].[18,19] However, the observed film regions did not show any tensile strains caused by the NGO substrate since it had been completely removed.

To properly understand our observations, we carried out further experiments by electron diffraction (ED) and electron holography.[20–23] Figure 2(a) displays a typical ED pattern viewed along the [010] direction and taken from the area with both types of magnetic domain walls, such as observed in Fig. 1(a) by LTEM. Interestingly, all Bragg's $(h0l)$ reflections including the central spot are magnetically split into couple of close spaced lines. Figure 2(b) shows the fine details of the incident-beam splitting, recorded with an aperture including two types of domains with dissimilar domain widths at a very large camera length. Intuitively, the magnetically split fine structure of the ED pattern can be thought as a result of Lorentz force deflections of the electrons as they go through a magnetized sample with a set of distinct directions of the magnetization. Typically, if **M** is the magnetization in an infinite domain, a spot is established in the diffraction pattern around $\mathbf{q}=(\mu_0 et/h)(\hat{\mathbf{z}}\times\hat{\mathbf{M}})$, where h is the Planck constant, e is the absolute value of the electron charge, and t is the film thickness. Ideally then, in a sample such as ours with four distinct directions of **M**, i.e., ±45° and ±135°, we should expect four spots, arranged on the vertices of a square. However, the ED pattern we acquired shows two split lines, each of them composed of several overlapping spots with different diffraction intensities [Fig. 2(b)]. Foucault images in Figs. 2(c) and 2(d) were recorded with the smallest available apertures in our microscope (10 μm in diameter) selected from two regions in Fig. 2(b) marked as A and B, respectively. These images depict three typical domain widths of about 50, 80, and 150 nm. Correlating the diffraction pattern and Foucault images, we found that magnetic origin of ED pattern fine structure [i.e., the two spotted lines in Fig. 2(b)] is directly related to the presence of alternating magnetic twin domains on either side of the zigzag domain walls and, therefore, cannot be attributed to simple (101) lattice twinning of the orthorhombic crystal film alone. The magnetic nature of ED pattern was further confirmed by heating experiments, when magnetically split diffraction pattern (DP) structure disappeared above the magnetic Curie point for LPCMO film retaining however nanocrystal twinning at higher temperatures due to persistent small orthorhombic distortion.

To investigate the relationship between the width of individual twin domains, the corresponding twist angle and the local induction within the twin magnetic domains, an area of the LPCMO sample far from the zigzag type domain wall was explored by scanning convergent electron diffraction.[19] We used the smallest available nanoprobe (~40 nm diameter for our LTEM), focusing it on the sample plane and recording the corresponding nanoarea electron-diffraction pattern as we scanned the beam along two orthogonal directions (as x scan and y scan), i.e., parallel to and perpendicular to the direction of the twin domain wall. For the sake of consistency, our choice of (x,y) directions in Fig. 2(e) and corresponding (q_x,q_y) directions in Fourier space for Fig. 2(b) will be used for the discussion below, which deviates from *hkl*-indexing directions for ED pattern in Fig. 2(a). By scanning the nanoprobe parallel (x scan) to the twinning domain wall while remaining in a single magnetic domain, we observed one single diffraction spot in the diffraction pattern that was fixed in reciprocal space relative to the transmitted beam shown by the open squares in Fig. 2(e). Conversely, scanning the probe perpendicular to the direction of the twining domain wall (y scan) again yielded a single diffraction spot but its position in reciprocal space oscillated as shown by the solid squares in Fig. 2(e).

To obtain reliable data, we scanned the focused beam back and forth throughout 12 domains. Apparently, the magnetic induction differs from domain to domain but is constant within each one. Furthermore, the magnetic induction varies with the domain width: the wider domains have a smaller magnetic induction component along q_y while it remains constant along q_x, as suggested by the straight lines observed in the diffraction patterns [see Fig. 2(b)] obtained from wide areas of view. At this stage, we can look for correlations between the ED pattern fine structure and the domain width. From real-space images [Fig. 1(a)] we know that the wider domains have some larger 2θ twist angle. Therefore, to correlate these observations, the six spots in each line of the split spot [Fig. 2(b)] were associated with different values of the twist angle θ: ±49° (spots 1 and 6); ±56° (spots 2 and 5); and ±75° (spots 3 and 4). While the first two values (spots 1, 2, 5, and 6) correlate well with the angles we measured earlier, the ±75° couple of spots do not. Further discussion on its possible origin follows below.

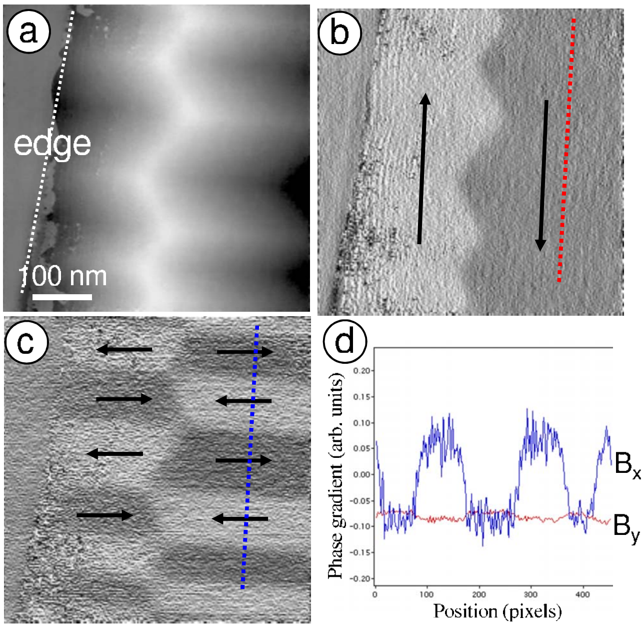

FIG. 3. (Color online) (a) Reconstructed electron-optical phase shift $\varphi(x,y)$ from off-axis electron hologram. (b) and (c), the two phase gradient components, are proportional to the y and x components of the local magnetic induction within the sample. (d) Profiles of B_y and B_x components extracted from the phase gradient.

In order to supplement and directly confirm the diffraction results presented above, we carried out electron holography experiments on the same LPCMO sample. An off-axis electron hologram was obtained from a region of the sample near the vacuum (i.e., edge of the sample), where both types of magnetic domain wall (twin and zigzag types) are present. Figure 3(a) is the reconstructed electron-optical phase shift $\varphi(x,y)$ reconstructed from the hologram. Figures 3(b) and 3(c) are the two components of the phase gradient $-\partial_y\varphi(x,y)$ and $\partial_x\varphi(x,y)$, and are proportional, respectively, to the in-plane magnetic induction components B_x and B_y projected along the beam path according to[24,25]

$$\partial_x\varphi(x,y) = \frac{2\pi e}{h}\int_{-\infty}^{+\infty} B_y(x,y,z)dz, \tag{1}$$

$$-\partial_y\varphi(x,y) = \frac{2\pi e}{h}\int_{-\infty}^{+\infty} B_x(x,y,z)dz. \tag{2}$$

In absence of stray fields above and below the sample, and assuming that the magnetic induction does not vary along z within the sample, the projected field is simply the product between sample thickness and local magnetic induction in the sample

$$\partial_x\varphi(x,y) = \frac{2\pi e t}{h}B_y(x,y), \tag{3}$$

$$-\partial_y \varphi(x,y) = \frac{2\pi e t}{h} B_x(x,y). \tag{4}$$

Figure 3(d) shows line profiles of the phase gradient along the dashed lines in Figs. 3(b) and 3(c). The profile across the twin domains for the B_y component in Fig. 3(d) is approximately constant, confirming the observations and conclusions drawn from the diffraction experiments summarized above.

The meander-shape profile for the B_x component across the twin domains in Fig. 3(d), however, does not show much variation between twin domains of similar widths as we anticipated. The reason for this is most likely a combination of factors owing to the experimental constraints associated with these holography experiments, i.e., only regions near the sample edge can be observed. Consequently, we were unable to obtain suitable regions where the twin domain width varied significantly over the field of view, which implies that the B_x component does not vary significantly as well nor could we obtain regions far from zigzag domain walls. This latter point is important since the zigzag domain walls might influence the measurements if they were not made far enough from these 180° domain walls. Nevertheless, the holography experiments directly indicate that the B_y component of the projected induction remains constant, consistent with results of the diffraction experiments described above.

IV. MODELING AND INTERPRETATION OF THE EXPERIMENTAL RESULTS

The various TEM techniques we used to examine the domain microstructure in LPCMO highlight several puzzling aspects of the FM domain microstructure in a material that shows a strong CMR effect.[1,2,12] Our observations suggest that at low fields the electron-spin scattering, and hence the magnetoresistance of LPCMO, should be a sensitive function to specific FM microstructure, characterized by very high density of twin magnetic domains ($\sim 2\times 10^5$ walls/cm), created and strongly pinned ($H_c \sim 1.2$ kOe) by heavy crystallographic lattice twinning along (101) planes due to orthorhombic a-lattice contraction with final mismatch of only $\sigma = (c-a)/a = 3.7\times 10^{-4}$ (or 0.037%), as follows from our data reported above. Our experimental results also suggest that the nanoscale FM domain structure in LPCMO deviates from the pattern of just four main directions of the magnetization ±45° and ±135° that one may expect from the crystal symmetry involved. However, four major magnetically split spots in a rectangular arrangement are indeed observable in our diffraction patterns [Fig. 2(b)]. Note that the **q** vector for the strong magnetic spot marked "1" in Fig. 2(b) appears to be close enough to the [100] direction of the Bragg's diffraction pattern shown in Fig. 2(a). This is somewhat consistent with the [100] easy magnetic directions suggested by the real-space domain observations in Fig. 1(a).

In order to interpret correctly how the fine structure we observed in the diffraction patterns arise, in particular, the establishment of several spots and diffuse scattering around them, we provide a set of image simulations based on electron optical and mathematical modeling of the interaction between fast electrons and the magnetic field of the sample. As a plane wave of electrons travels through a region of space where electromagnetic fields exist, it acquires a phase modulation that is proportional to the scalar electrostatic and vector magnetic potentials[23,24,26]

$$\varphi(x,y) = C_E \int_{-\infty}^{+\infty} V(x,y,z)dz - \frac{2\pi e}{h}\int_{-\infty}^{+\infty} A_z(x,y,z), \tag{5}$$

where C_E is a prefactor that depends on the accelerating voltage and A_z is the component of the vector potential that is parallel to beam direction. Experimental observation suggests that little or no variation in the specimen thickness occurs and that no electric charges are involved. Therefore, the first term in Eq. (5) contributes to the common electrostatic phase offset that is not essential to our analysis. The second term, reflecting the magnetic contribution to the phase shift, may also be written as

$$\varphi(x,y) = -\frac{\pi}{\phi_0}\int\int \mathbf{B}_\perp \cdot d\mathbf{S}, \tag{6}$$

where $\phi_0 = 2.07\times 10^{-15}$ T nm^2 is the flux quantum, $\mathbf{B}_\perp$ stands for the two planar z-independent components of the magnetic induction, and, in the assumption of vanishing stray fields above and below the specimen, the integral represents the magnetic flux through the sample cross section at some location (x,y). The consistency between Eq. (6) and Eqs. (3) and (4) can be checked by carrying out a gradient operation.

As shown in Figs. 4(a)–4(d), phase and image simulations[25,27] calculated according to Eq. (6) agree well with the experimental results we obtained. In Fig. 4(a), we simulated an out-of-focus (Fresnel) image that reproduces well the observations reported in Fig. 1(a). In Figs. 4(b)–4(d), the phase shift $\varphi(x,y)$ and the two components of its gradient to be compared with the holographic maps in Figs. 3(b)–3(d). The simulated ED pattern [Figs. 4(f) and 4(h)] of the domain structure is calculated as the Fourier transform of the exit wave $\exp[i\varphi(x,y)]$ and magnified ~25× to fit the camera length used in the experiment. For comparison with experimental data (Figs. 1–3) we assigned a width of 50 nm to the domains and included the effects of a smooth variation in the magnetization across a domain wall over a region of 10 nm, mimicking a Bloch domain wall. The zigzag walls in this model are generated automatically at the surface intersection line between positive/negative slopes of the phase map separating positive (white) and negative (black) domains in the B_y component [Fig. 4(d)]. Notice that we used Maxwell equation $\mathbf{B} = \mu_0(\mathbf{M}+\mathbf{H}_d)$ for simplified description of the magnetic domains shown in Figs. 4(c) and 4(d). We also assume that ratio $M_y/M_x \sim 1$ remains fixed to keep the 90° twist angle for spin moments across (101) twist boundaries. By neglecting first with demagnetizing field H_d, the induction components B_y/B_x [see Figs. 4(c) and 4(d)] become simply proportional to magnetization components M_y/M_x. For this simple case of zero stray field ($H_d=0$) our model predicts ($2\theta = 90°$) twist angles anticipated for zigzag walls. To model larger twist angles ($2\theta > 90°$) observed in the remnant state of LPCMO, we took into account the de-

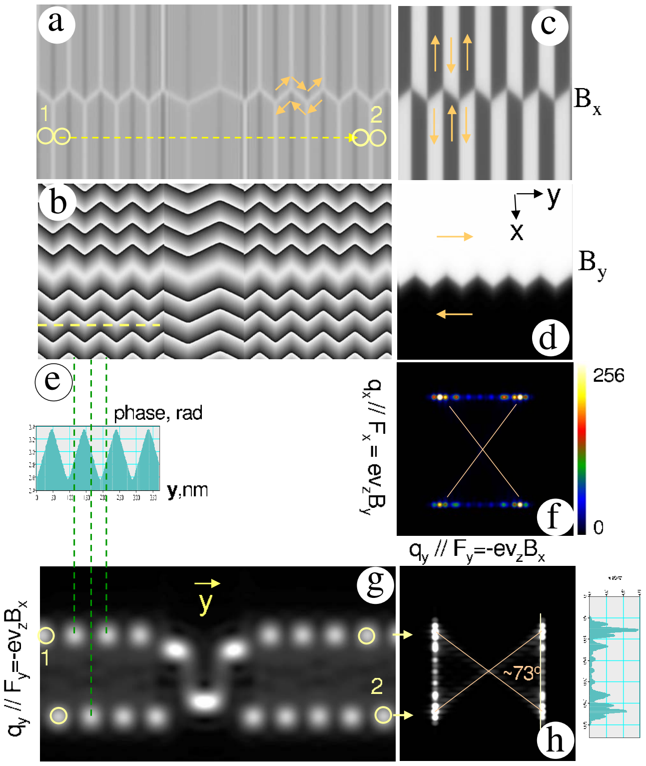

FIG. 4. (Color online) (a) Simulated Fresnel image for the zigzag and twin magnetic domain walls in LPCMO. (b) Wrapped phase map (4× amplified) $\varphi(x,y)$ of the complex exit wave for the set of magnetic domains. [(c) and (d)] Projected magnetic induction maps for the two orthogonal components (c) $B_x(x,y)$ and (d) $B_y(x,y)$ within the sample, derived from the phase gradient. (e) Line profile of the phase shift across the dashed line in (b) showing the typical smoothed sawtooth function associated to realistic magnetic domains. (f) Simulated diffraction pattern showing the fine structure of the magnetically split Bragg spot obtained by the Fourier transform of exit wave function $\exp[i\varphi(x,y)]$. (g) Simulation of a nanobeam scan across the twin domains along the dashed line in (a), to be compared with the experimental data shown in Fig. 2(e); the reciprocal coordinates and amplitudes of the diffraction spots resulting from the simulated y scan show how the fine structure of the composite diffraction pattern shown in (h) [obtained by 90° rotation of (f)] may arise.

magnetization field correction heuristically by assuming that $\mu_0H_d/B_x \sim 25\%$ (a demagnetization field along the x direction equal to one fourth of the induction x component; no demagnetization correction is needed for the B_y component), thus reducing accordingly $B_x = \mu_0(M_x - H_d)$ for the "head-to-head" and "tail-to-tail" magnetic domain walls marked in Fig. 4(c) with arrows. Consequently, the ratio B_y/B_x results in a twist angle increase up to $2\theta = 2\arctan(B_y/B_x) = (180 - 73) \sim 107°$. The effects of demagnetization fields will be further discussed below.

To reproduce the nanobeam scanning experiments in Fig. 2(e), we have computed the nanobeam y scan shown in Fig. 4(g) along the $1 \rightarrow 2$ path in Fig. 4(a). From the comparison between data and simulations, we conclude that nanobeam deflections in Fig. 2(e) and model Fig. 4(g) follow the Lorentz deflection force $F_y = -ev_zB_x(X,y)$ (X denotes the position where the line scan is taken) making nanoprobe a very sensitive tool for local induction mapping. The comparison between the composite DP in Fig. 4(h) versus nanobeam pattern in Fig. 4(g) highlights the fact that a real DP is more complex than a set of sharp spots associated to a given direction of the local magnetic induction. In fact, the real DP contains interference effects from several magnetic domains scattering coherent electrons at the same time. Nonetheless, the two strongest spots in each quadrant of the DP in Fig. 4(h) remain consistent with two major nanobeam deflections for narrow and wide domains shown in Fig. 4(g). From our analysis it follows that the fine structure of the magnetically split Bragg reflection spot as illustrated in Fig. 2(b), and Fig. 4(h) follows from the condition of constant B_y component [Fig. 4(d)] for all types of twin domains, resulting in constant Lorentz deflection parallel to q_x. Meanwhile, each twin domain may have a particular B_x component dictated by its own shape, in turns caused by heavy crystal (101) twinning that contributes with variable Lorentz deflection to the spotted lines along q_y.

To further investigate the effects of demagnetization fields, we carried out another set of simulations where the complex domain pattern is described as a suitable superposition of rectangular magnetized elements of a given aspect ratio. In this perspective, while we neglect the presence of domain walls and the establishment of the zigzag twinning pattern, the demagnetization fields arise naturally from the particular domain shape and orientation of its magnetization. The basic building block that enables us to reproduce the distribution of the magnetic field associated with the set of twins is a uniformly magnetized rectangle, wherein the magnetization forms an angle β with respect to the horizontal nanotwins direction (taken as the x axis). The phase shift associated to a uniformly magnetized rectangle can be computed analytically (see, e.g., Refs. 24 and 28). As shown in Fig. 5(a), by arranging suitably a number of rectangular elements, each with its own aspect ratio and magnetization orientation, we can produce an overall phase distribution based on our experimental data above.

Inspection of Fig. 5(a), where we simulate 20 narrow domains (aspect ratio 6:1) and two larger central domains (aspect ratio 3:1), reveals that the inclination of the phase contour fringes depends on the domain aspect ratio as well as on the overall geometry of the set of twins (i.e., the distance from the edges and the total number of domains within the simulation region). It is important to note that the simulations presented in Fig. 5 assume that the individual domains are magnetized along the magnetic easy axes of the LPCMO, i.e., along the ⟨100⟩ directions forming 90° domain walls across the twin boundaries (this configuration corresponds to $\beta = \pm 45°$). The simulated diffraction pattern, Fig. 5(b), is consistent with earlier considerations and with the experiments. The complex pattern, that differs from the simplistic expectation of four isolated spots, contains a wealth of information: each spot is elongated, representing a degree of variation in the orientation of the local magnetic induction within the domains due to nonuniformities caused by the presence of local demagnetized fields. This demonstrates the combined effect of the magnetic-moment distribution and any demagnetizing fields associated with the magnetic-moment distribution. Also, the additional demagnetization

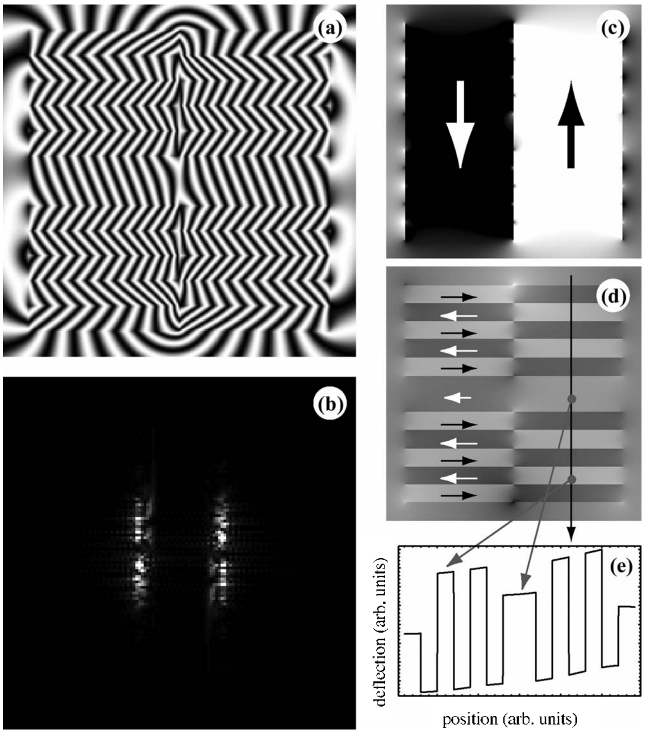

FIG. 5. (a) Electron-optical phase shift, displayed as a cosine map, associated with a double set of twins (20 narrow domains with a 6:1 aspect ratio and two broader domains with aspect ratio of 3:1); (b) simulated diffraction pattern associated with the double set of twins; (c) phase derivative along the horizontal direction, related to the projected B_y component; (d) phase derivative along the vertical direction, related to the projected B_x component; and (e) vertical line profile across the B_x map, proportional to the electron deflection.

effects near the lateral edges introduce further changes in orientation that again are visible in the diffraction patterns. We also show the x and y components of the phase gradient [Figs. 5(c) and 5(d), respectively]. Recalling the proportionality between phase gradient and local projected induction, Eqs. (3) and (4), we confirm that while the B_y component is roughly constant across the twin domains independent of domain width, there is a difference in the B_x component between the 6:1 and 3:1 domains: this is what establishes the different inclination of the phase contour fringes in Fig. 5(a). As the projected induction is also directly related to the electron deflection,[29] we can take a vertical line profile across the B_x map and compare it with results of diffractive imaging shown in Fig. 2(b). We note, in particular, that the simulated deflection of the beam appears smaller when associated with the broader domains, exactly as observed in the diffraction experiments.

V. CONCLUSION

In summary, the structural feature and spin configuration of the two sets of magnetic domain walls, twinning and zigzag types, in $La_{0.325}Pr_{0.3}Ca_{0.375}MnO_3$ films have been studied by integrated low-temperature electron microscopy methods below the FM to AFM transition temperature. We found that in FM state magnetic spin moments of twinning domains coincide with easy crystallographic (a or c) axes of crystal (101) twins in LPCMO by creating zigzag configurations for head-to-tail magnetic moments with 90°-twist angle when crossing (101) twin boundaries. However, "observable" magnetic directions measured by means of projected magnetic induction in TEM may vary significantly from 90° to 120°, depending on local geometry of crystal-twin lamellae carrying magnetic moments, in particular, their width and aspect ratio. The origin of such deviations for observable projected magnetic induction from easy magnetic directions aligned with crystallographic axes of LPCMO is attributed to local effects of demagnetizing fields associated with nonuniform shapes of very small ($\sim 50-100$ nm) nanocrystalline (101) twins found in FM state of LPCMO below Curie temperature.

It is interesting to note that the two type of domains respond very differently when an external magnetic field is applied: the twinning type domain walls are strongly pinned to the (101) twin boundaries while the zigzag type domain walls are very mobile. The movement of the zigzag walls alters the aspect ratio of the individual domains yielding considerably different local induction B fields from equilibrium magnetic moments of the material. This might be one of the key ingredients driving the most dramatic changes for CMR phenomenon in doped manganites at low and moderate magnetic fields. We expect that our findings can be generalized to additional ferromagnetic systems with strongly correlated electrons, where the magnetic domain structure will depend sensitively on the crystallographic geometry of the material and where the balance between distinctly different types of domain walls might lead to dramatical changes in scattering mechanism for conduction electrons in CMR material upon application of magnetic field.

ACKNOWLEDGMENTS

This work at BNL was supported by the U.S. Department of Energy, Office of Basic Energy Science under Contract No. DE-AC02-98CH10886. We thank S. Chaudhuri and R. C. Budhani for providing samples.

---

[*] Corresponding author; jiaqing-he@northwestern.edu

[1] E. Dagotto, New J. Phys. **7**, 67 (2005).
[2] M. Uehara, S. Mori, C. H. Chen, and S.-W. Cheong, Nature (London) **399**, 560 (1999).
[3] J. C. Loudon, N. D. Mathur, and P. A. Midgley, Nature (London) **420**, 797 (2002).
[4] S. Chaudhuri, R. C. Budhani, J. Q. He, and Y. M. Zhu, Phys. Rev. B **76**, 132402 (2007).
[5] J. Q. He, J. C. Zheng, S. Chaudhuri, R. C. Budhani, and Y. M. Zhu, J. Appl. Phys. **103**, 064304 (2008).

[6] T. Asaka, Y. Anan, T. Nagai, S. Tsutsumi, H. Kuwahara, K. Kimoto, Y. Tokura, and Y. Matsui, Phys. Rev. Lett. **89**, 207203 (2002).

[7] T. Asaka, T. Kimura, T. Nagai, X. Z. Yu, K. Kimoto, Y. Tokura, and Y. Matsui, Phys. Rev. Lett. **95**, 227204 (2005).

[8] S. J. Lloyd, N. D. Mathur, J. C. Loudon, and P. A. Midgley, Phys. Rev. B **64**, 172407 (2001).

[9] G. Jung, V. Markovich, D. Mogilyanski, C. Van der Beek, and Y. M. Mukovskii, J. Magn. Magn. Mater. **290-291**, 902 (2005).

[10] P. Schiffer, A. P. Ramirez, W. Bao, and S. W. Cheong, Phys. Rev. Lett. **75**, 3336 (1995).

[11] G. Tatara and H. Fukuyama, Phys. Rev. Lett. **78**, 3773 (1997).

[12] M. A. Schofield, J. Q. He, V. V. Volkov, and Y. Zhu (unpublished).

[13] Q. Lu, C. C. Chen, and A. De Lozanne Science **276**, 2006 (1997).

[14] T. Fukumura, H. Sugawara, T. Hasegawa, K. Tanaka, H. Sakaki, T. Kimura, and Y. Tokura, Science **284**, 1969 (1999).

[15] A. Gupta, G. Q. Gong, G. Xiao, P. R. Duncombe, P. Lecoeur, P. Trouilloud, Y. Y. Wang, V. P. Dravid, and J. Z. Sun, Phys. Rev. B **54**, R15629 (1996).

[16] Y. Wu, Y. Suzuki, U. Rüdiger, J. Yu, A. D. Kent, T. K. Nath, and C. B. Eom, Appl. Phys. Lett. **75**, 2295 (1999).

[17] M. A. Schofield, M. Beleggia, Y. Zhu, and G. Pozzi, Ultramicroscopy **108**, 625 (2008).

[18] A. M. Haghiri-Gosnet and J. P. Renard, J. Phys. D: Appl. Phys. **36**, R127 (2003).

[19] J. Dho, Y. N. Kim, Y. S. Hwang, J. C. Kim, and N. H. Hur, Appl. Phys. Lett. **82**, 1434 (2003).

[20] J. Tao, D. Niebieskikwiat, M. Varela, W. Luo, M. A. Schofield, Y. Zhu, M. B. Salamon, J. M. Zuo, S. T. Pantelides, and S. J. Pennycook, Phys. Rev. Lett. **103**, 097202 (2009).

[21] *Introduction to Electron Holography*, edited by E. Volkl, L. F. Allard, and D. C. Joy (Plenum Press, New York, 1999).

[22] M. A. Schofield, M. Beleggia, Y. M. Zhu, K. Guth, and C. Jooss, Phys. Rev. Lett. **92**, 195502 (2004).

[23] P. A. Midgley, Micron **32**, 167 (2001).

[24] M. Mankos, M. R. Scheinfein, and J. R. Cowley, Adv. Imaging Electron Phys. **98**, 323 (1996).

[25] V. V. Volkov and Y. Zhu, Phys. Rev. Lett. **91**, 043904 (2003).

[26] Y. Aharonov and D. Bohm, Phys. Rev. **115**, 485 (1959).

[27] V. Volkov and Y. Zhu Ultramicroscopy **98**, 271 (2004).

[28] P. F. Fazzini, G. Pozzi, and M. Beleggia, Ultramicroscopy **104**, 193 (2005).

[29] M. Beleggia, M. A. Schofield, Y. Zhu, and G. Pozzi, Ultramicroscopy **310**, 2696 (2007).